Appl Phys A (2013) 110:343–350
DOI 10.1007/s00339-012-7264-0

Applied Physics A
Materials Science & Processing

Ligand-free gold–silver nanoparticle alloy polymer composites generated by picosecond laser ablation in liquid monomer

Ana Menéndez-Manjón · Andreas Schwenke · Timo Steinke · Matthias Meyer · Ulrich Giese · Philipp Wagener · Stephan Barcikowski

Received: 11 May 2012 / Accepted: 9 September 2012 / Published online: 29 September 2012

Abstract Polymer matrix nanocomposites filled with metallic and alloy nanoparticles add functionality in various applications such as optical devices and in the energy sector. However, matrix coupling agents or nanoparticle ligands may be unwanted additives, potentially inhibiting the resulting nanocomposite to be processed by injection molding. The generation of stabilizer-free Au, Ag, and AuAg alloy nanoparticle acrylate composites is achieved by picosecond-pulsed laser ablation of the respective metal target in the liquid monomer. Complementary to laser ablation of the solid alloy, we have alloyed nanoparticles by post-irradiation of Au and Ag colloids in the liquid monomer. The optical properties of the colloidal nanoparticles are successfully transferred to the solid poly(methyl methacrylate) matrix and characterized by their plasmon resonance that can be easily tuned between 400 and 600 nm by laser alloying in the liquid monomer.

1 Introduction

Polymer matrix composites filled with metallic nanoparticles are implemented in gas sensors [1], solar cells [2], packaging [3], flame retardants [4, 5], stimuli-responsive devices [6], and optoelectronic devices [7]. Many methods are applied to disperse nanoparticles in a polymer. Fillers can be incorporated in the polymer matrix via physical or chemical methods, and via wet or dry synthesis, with or without cross-linker components [8]. The uniform dispersion of nanoparticles in the polymer bulk is one of the most challenging aspects of nanocomposite production [9]. Pulsed laser ablation (PLA) of solid targets in liquids has been established as a novel route to nanoparticle generation, where the particle size distribution can be controlled by using the appropriate laser parameters [10–13] and physicochemical properties of the liquid [14–17]. This technique enables the generation of nanoparticles directly in a monomer [18] or in organic solutions containing polymer stabilizers, such as polyoamidoamine dendrimers [19] or thiol-functionalized polymers [20]. Besides the stabilizing effect, the nanoparticle surface may be functionalized when block polymers or end-functionalized polymers are employed, which increases the compatibility to polymer matrices, thereby enhancing dispersion of nanoparticles in the final nanocomposite. The in-situ generation and functionalization of nanoparticles by pulsed laser ablation facilitates the integration of nanomaterials in the polymer matrix and reduces agglomeration, guaranteeing that the filler's properties take maximal effect in the polymer matrix. Moreover, short laser pulses permit the most efficient ablation of almost any material [21], with low or no thermal load on the target [22]. This principally facilitates a stoichiometric ablation of alloyed materials [23, 24] without degradation of the solvents or contained molecules [25].

Metallic and bimetallic nanoparticles attract considerable attention for their tunable electrical, optical, or thermal properties. The modulation of these properties can be realized via varying the size, shape, composition, and

A. Menéndez-Manjón · A. Schwenke
Laser Zentrum Hannover e.V., Hollerithallee 8, Hannover 30419, Germany

T. Steinke · M. Meyer · U. Giese
Deutsches Institut für Kautschuktechnologie e.V., Eupener Straße 33, Hannover 30519, Germany

P. Wagener · S. Barcikowski (✉)
Technical Chemistry, University of Duisburg-Essen and Center for Nanointegration Duisburg-Essen (CeNiDE), Duisburg, Germany
e-mail: stephan.barcikowski@uni-due.de

structure (alloy or core–shell) of the nanoparticles. It has been shown that a combination of Au and Ag depresses the microbial proliferation below the levels reached with Ag-nanocomposites only [26]. Au, Ag, and AuAg alloy nanoparticles find applications in medicine, such as antibacterial catheters [26], and specifically embedding a combination of Ag and Au nanoparticles in polymer triggers electrochemical reactions that allow tuning of an ion release [27]. Furthermore, alloy nanoparticles enhance the performance of hydrogen fuel cells, and are applied in catalytic electrodes [28]. Especially interesting is the inclusion of metallic nanocomposites in photonic devices, due to their photostability, and in laser technology where they may be implemented in optical limiters [29] and safety goggles. Homogeneous particle dispersion in the solid is a prerequisite for many applications. To this end, we recently investigated the optimal polymer concentration in organic liquid at which there is minimal aggregation of nanoparticles in the solidified nanocomposite derived from PLA in a polymer solution [30].

It has recently been shown that PtIr and magnetic NiFe alloy nanoparticles can be fabricated by PLA in an organic liquid [31, 32], and the in-situ generation of nanoparticles by laser ablation in monomers provides base-materials for a rapid prototyping of nanocomposites. In the present work, we demonstrate a one-step process for the generation of metallic (Au and Ag) and alloy (AuAg) polymer nanocomposites, with poly(methyl methacrylate) (PMMA) as polymer matrix.

2 Experimental section

Nanoparticles were generated by pulsed laser ablation of Au, Ag, and AuAg-alloy solid foils of 1 mm thickness (99.99 %, Goodfellow) in methyl methacrylate (MMA, 99.99 %, Fluka). The atomic composition of the AuAg-alloy is 52.98 % Au and 47.02 % Ag, determined by energy-dispersive X-ray spectroscopy (EM 10 C, Zeiss). A self-designed ablation chamber with a rotating motor has been used as container in order to induce a continuous circular flow of the liquid during the laser ablation process (Fig. 1). The targets where fixed inside the chamber, parallel to a laser entrance quartz-window (at a distance of 5 mm) and perpendicular to the laser beam. The chamber was filled with 33 ml MMA for each experiment. A picosecond-pulsed laser system (TruMicro 5250, Trumpf) delivering 125 µJ pulses of 7 ps pulse duration at a repetition rate of 33.3 kHz with a wavelength of 515 nm was used for the ablation. The laser beam (10 mm diameter) was guided by mirrors to an optic scanner (HurryScan II 14, Scanlab) and focused via a F-Theta lens (56 mm focal length). The chamber was positioned along the laser propagation direction with a translation stage. The relative distance between lens and target was

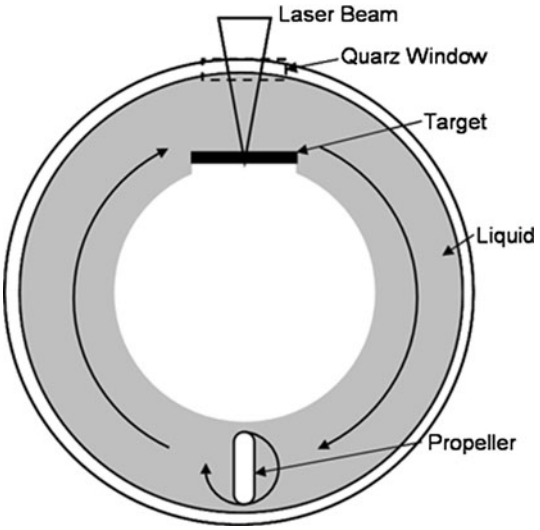

Fig. 1 Top view of the experimental set-up for laser ablation in flowing liquid designed for generating nanoparticles

optimized for obtaining the maximal ablated mass, which was determined gravimetrically. The lens-target distance was kept constant during the ablation of all three different targets. The laser beam was scanned in a spiral pattern with 5 mm diameter and 50 µm line distance at a scanning speed of 3.3 m/s, resulting in an interpulse distance of 100 µm. Ablation was performed for 10 min for each sample. The plasmon absorption band of the nanoparticles in the colloidal dispersion and in the polymer matrix were determined by UV-Vis spectroscopy (UV-1650PC, Shimadzu). The hydrodynamic size distribution of the nanoparticles dispersed in the monomer solution was determined using dynamic light scattering operated at a wavelength of 633 nm (Zetasizer Nano, Malvern Instruments Ltd.).

After the generation of nanoparticles in the monomer, the colloids were mixed with 1 ml 0.1 wt% azo-bis-(isobutyronitrile) followed by heating in a glass bottle to 80 °C for 30 min. The resulting nanocomposite samples can be seen in Fig. 3(b).

The size distribution of primary nanoparticles embedded in poly(methyl methacrylate) (PMMA) was measured by transmission electron microscopy (Libra120, Zeiss). Because of statistical requirements, over 400 nanoparticles were counted in each sample. The atomic composition of single nanoparticles was determined by FE–STEM–EDXS (field emission–scanning transmission electron microscopy–energy dispersive X-ray spectroscopy, JEM-2100F, JEOL Ltd.).

Laser-generated Au and Ag nanoparticles dispersed in MMA were mixed and reirradiated for 15 min with the same laser parameters that were used for the ablation process. The focus of the laser was positioned in the middle of the liquid layer (8 mm depth).

Table 1 Mass concentration of each material after 10 min of laser ablation and calculated reflectance of the targets a wavelength of 532 nm

	Ag	AuAg	Au
Concentration (μg/ml)	40.5	73.3	84.6
R^a	0.97	0.64	0.33

[a]The refractive index values were taken from: Phys. Rev. B **6**(11), (1972) 4370–4379

3 Results and discussion

3.1 Concentration and productivity

During the laser ablation process in MMA coloring of the solution was observed, intense yellow, orange and red colors, characteristic for colloidal silver and gold nanoparticles. The concentration of nanoparticles in the colloids was determined from the ablated mass. It is assumed that the ablated material is completely dispersed in the liquid since no deposition of nanoparticles is observed on the target or chamber walls. The flowing liquid over the target surface improves the nanoparticle productivity, since the ablation process becomes more stable and effective because formed nanoparticles are carried away by the flow from the ablation site [33]. Ablation rates of 8, 14.5, and 16.7 mg/h for Ag, AuAg, and Au were reached under the employed experimental conditions. The mass concentrations produced by ablation of each solid target are listed in Table 1. The lower ablated mass observed for Ag compared to the AuAg-alloy and Au can be understood when considering the higher reflectance of the Ag at the incident wavelength. The reflectance values presented in Table 1 were calculated with the Fresnel equation for normal incidence [34]. Since the dielectric function of the metal alloys can be expressed as the composition-weight average of the dielectric functions of the constituent elements $\varepsilon = x\varepsilon_1 + (1-x)\varepsilon_2$ [35–38], with x the molar fraction and ε_1 and ε_2 the composing dielectric functions, the reflectivity continuously varies between the values of Au and Ag [39].

The productivities and concentrations achieved here provide competition for existing processing methods. For example, ablating gold in MMA for 12 min will produce enough nanoparticles to create 32 optical filters (1 inch diameter and 2 mm thickness) with $T = 50$ % at the plasmon resonant wavelength.

It must be noted that the maximum nanoparticle concentration that can be achieved is potentially limited by absorption and scattering of the incoming laser beam by nanoparticles already present in the solution. In a recent study, it was demonstrated that plasmon-resonant nanoparticles inhibit the productivity when a laser excitation wavelength is used close to the wavelength at which the nanoparticles absorb [40].

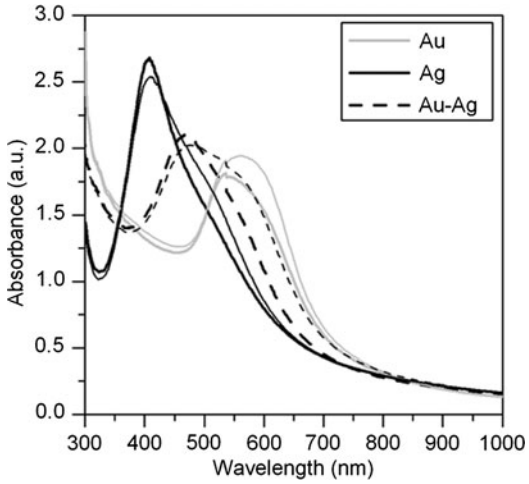

Fig. 2 Plasmon resonance spectra of the colloidal dispersions. Spectra of Au, Ag, and AuAg nanoparticles generated by picosecond laser ablation in methyl methacrylate. *Thinner lines* represent the spectra of the colloidal solutions 12 h after production

3.2 Plasmon resonance and nanoparticle dispersion in monomer and polymer

UV-Vis measurements were carried out to assess the embedding of the nanoparticles into the polymeric matrix and to evaluate whether ripening or aggregation of nanoparticles occurred over time. The UV-Vis absorption spectra of the Au, Ag, and AuAg nanoparticles in MMA were measured in solution before polymerization and are shown in Fig. 2. The gold nanoparticles prepared in MMA by PLA present a broad plasmon peak centered at 543 nm, measured immediately after the ablation process. Mie theory predicts that such a plasmon band is caused by a broad size distribution of nanoparticles, where not only absorption but also light scattering contributes to the extinction spectrum [41]. The plasmon band absorption of Ag nanoparticles is narrower and centered at 406 nm indicating that smaller spherical nanoparticles are dispersed in the liquid. An incipient relative maximum at 515 nm in the extinction spectrum shows that also big Ag nanoparticles or agglomerates form part of the colloidal system.

Besides size and morphology of nanoparticles, information about the composition and structure can be derived from their plasmon resonances. When an Au and Ag colloid in MMA are mixed, two different plasmon resonant wavelengths are recognized in the spectrum of the colloid, one near 400 nm for the Ag nanoparticles and a second one around 500 nm for the Au nanoparticles (see Fig. 8). The proportion between these plasmon bands is related to the particle concentration of each population in the resulting colloid [42]. In contrary, nanoparticles generated by ablation of the AuAg alloy present a single resonant peak at 467 nm, between the Au and Ag nanoparticles plasmon bands. This

indicates that the nanoparticles obtained by the ablation of the alloy target are spherical and conformed by a mixture of Au and Ag, i.e., there are no individual Au and Ag nanoparticles. A homogeneous distribution of these elements in the nanoparticles is also expected. If, for example, a core–shell structure results from the alloy ablation, the plasmon peak would be centered at the plasmon wavelength of the core. The increment of shell thickness would only induce a damping of the core plasmon band.

The plasmon absorption bands of the laser-generated colloids were measured 12 h after their generation (thin lines in Fig. 2) in order to test the stability of the nanoparticles in MMA. It can be seen in Fig. 2 that the plasmon peaks shift to longer wavelengths and become broader with time in the three colloidal solutions. Furthermore, absorbance in the UV region, proportional to the Ag and Au atomic concentration due to interband transitions, remains unchanged. This indicates that nanoparticles grow trough Ostwald ripening or agglomerate forming clusters, but do not sediment. The ablated material is completely dispersed in the monomer matrix.

After polymerization, the UV-Vis spectra were measured in different positions of the nanocomposites in order to test the homogeneity of the nanoparticle distribution in the polymer volume. The standard deviation from the average plasmon peak is indicated by the line thickness in Fig. 3. A comparison with plasmon bands of colloids obtained by laser ablation (Fig. 2) shows that the characteristic plasmon bands, and hence the colloidal optical properties, are successfully transferred to the PMMA matrix. The higher spatial variation of the optical properties in the Ag nanocomposite might be caused by increased aggregation of the nanoparticles in the polymer matrix, visible to the naked eye. The lower degree of inhomogeneity in the Ag-composite compared to the other two composites can be seen in the photos in Fig. 3.

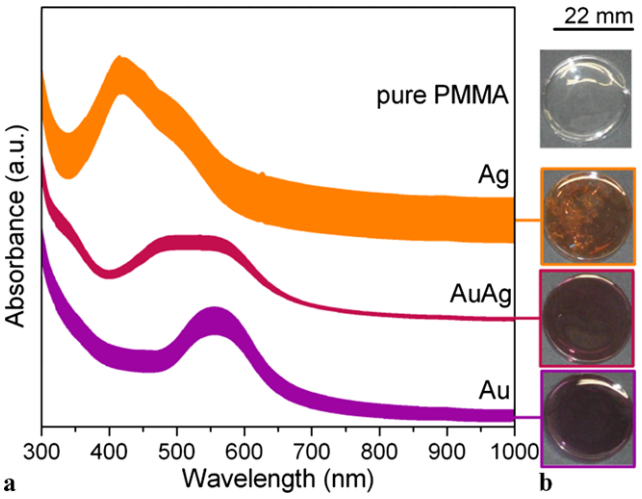

Fig. 3 Absorption spectra (**a**) of laser-generated Ag, AuAg, and Au PMMA nanocomposites. The line thickness represents the absorbance deviation at different localizations of the nanocomposite plates. (**b**) The three different synthesized nanocomposites as well as pure polymer (PMMA). The reference polymer is shown for comparison

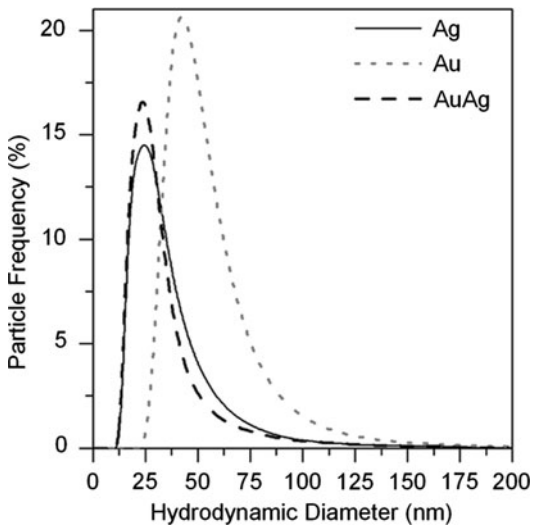

Fig. 4 Hydrodynamic diameter size distribution of Ag (*black line*), Au (*dotted line*) and AuAg (*dashed line*) nanoparticles fabricated by picosecond laser ablation in MMA

3.3 Particle size distribution

Dynamic light scattering enables the characterization of the dispersion of nanoparticles in liquids. The hydrodynamic diameter size distributions of the colloids formed using laser ablation of solid targets in MMA were determined by this method immediately after the ablation process. The results are shown in Fig. 4. It can be seen that Ag and AuAg nanoparticles have a similar size distribution, having a mean hydrodynamic diameter of 28 and 30 nm, respectively. The Au nanoparticles are bigger, with a mean hydrodynamic diameter of 50 nm. Dynamic light scattering measurements are based on the autocorrelation function of fluctuations of scattered laser signal resulting from the Brownian motion of the particles. As nanoparticles have a solvation layer, the diffusion coefficient is smaller than for "naked" particles and particles appear bigger than they in fact are. Moreover, this technique is based on Mie-scattering of a laser beam by nanoparticles, and the scattered intensity scales with d^6, where d is the particle diameter. The signal produced by 10^3 nanoparticles of diameter 5 nm would be needed to produce the same signal intensity of only one particle of 15 nm. For this reason, big nanoparticles or agglomerates of particles mask the weak signal coming from small primary particles. Hence, the hydrodynamic diameters measured are relatively small compared to the observed agglomerates by electron microscopy (of 50–100 nm typical Feret diameter (the largest distance of two tangents to the contour of the measured particle)), allowing to conclude that the nanoparticles can be found mainly finely dispersed and isolated in

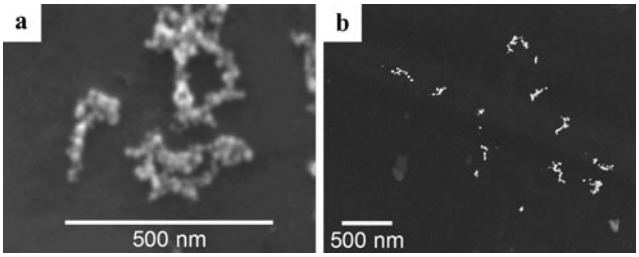

Fig. 5 Nanoparticle clusters observed by TEM imaging of the laser-generated Ag colloids in MMA (**a**), and by STEM imaging of the AuAg PMMA nanocomposite (**b**)

MMA after the ablation process. The formation of agglomerates is probably induced during the polymerization and drying of the colloidal solutions during sample preparation for electron microscopy. The material properties displayed by nanocomposites are strongly influenced by the size of nanoparticles. For a proper characterization of nanocomposites produced by laser ablation, the size distribution and dispersion of nanoparticles in PMMA were determined by transmission electron microscopy and are shown in Figs. 5 and 6. Additional to Fig. 5, in Fig. 7, it can also be seen that the nanoparticles are arranged in aggregates that are homogeneously distributed throughout the polymer matrix. Laser-generated nanoparticles usually present a lognormal distribution with a long tail extending to bigger particles. The origin of the formation of larger particles has been attributed to plasma-supported ablation for ultrashort laser pulses and can be suppressed by reduction of the laser fluence [10, 13]. The particles obtained here also present a lognormal distribution in the case of monomodal distributions (Au nanoparticles). Bimodal size distributions were detected for Ag and AuAg nanoparticles. The Au nanoparticles show a bigger mean diameter (11.1 nm) compared to Ag (8.6 nm) and AuAg nanoparticles (10.5 nm), however, all particles are smaller than 35 nm. The same tendency is found for the hydrodynamic and Feret diameter of primary particles, confirming that the DLS technique showed principally finely dispersed particles in the solution.

Different particle size distributions for Au and Ag or AgAu nanoparticles can be caused by laser-induced particle fragmentation [43]. As nanoparticles are dispersed in the liquid during the generation process; successive laser pulses reirradiate them. It has been shown that the absorption of laser irradiation by colloidal particles induces their fragmentation [44, 45]. Due to this post-irradiation and subsequent fragmentation, the particle size distribution shifts towards smaller particles [40]. Gold and silver nanoparticles efficiently absorb light in the visible range because of plasmon resonances at their surface. The plasmon band absorption of spherical gold nanoparticles in PMMA is estimated by Mie-theory (for particles with $r < 10$ nm) to be at 572 nm, while

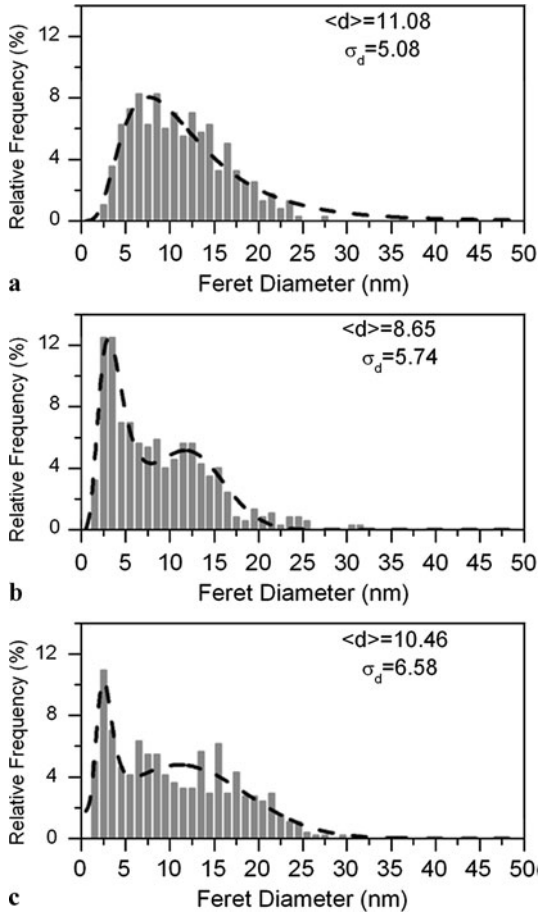

Fig. 6 Particle size distributions measured by TEM imaging of Au (**a**), Ag (**b**), and AuAg nanoparticles (**c**). Feret diameter: the largest distance of two tangents to the contour of the measured particle

for silver it is found at 406.5 nm [46].[1] The plasmon peak continuously shifts to longer wavelengths as the particle size increases. Each specific size range will therefore preferably absorb a determined wavelength. For this reason, large Ag nanoparticles or agglomerates, which efficiently absorb the 515 nm laser radiation, are heated and fragmented. As consequence, the size distribution of Ag nanoparticles is dynamically modified during the generation process, and small spherical dispersed nanoparticles are formed from the ablation plume, simultaneously with fragmentation of bigger particles dispersed in the liquid. In the case of Au nanoparticles, the bigger particles absorb further from the laser wavelength (over 600 nm), so a much less efficient fragmentation occurs for the Au nanoparticles. This explains also the bimodality of the distributions of Ag and AuAg nanoparticles. Only a fraction of the generated nanoparticles is fragmented

[1] For the calculation of the plasmon wavelength, the following material parameters are used: refractive index of MMA $n_{\mathrm{MMA}} = 1.49$; plasma frequency of Au $\lambda_p = 136.3$ nm; plasma frequency of Ag $\lambda_p = 133.0$ nm (Landolt–Börnstein); high frequency dielectric function of Au 13.2 nm and Ag 4.9 nm.

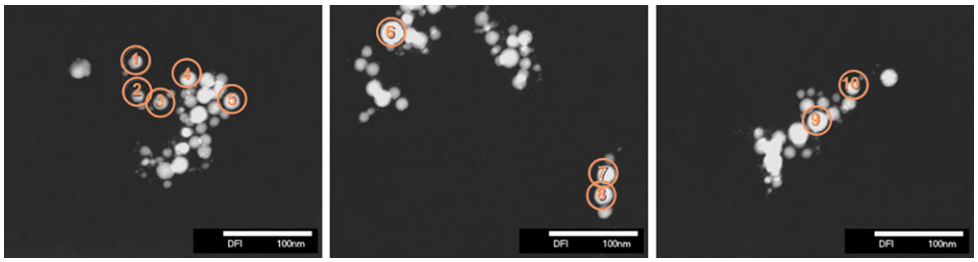

Fig. 7 AuAg-Nanoparticles in poly(methyl methacrylate) analyzed by FE-STEM-EDXS

by the laser, thereby increasing the population of small particles. The big size population, which is not affected by the laser wavelength, remains unchanged.

3.4 Nanoparticle stoichiometry

To verify the formation of AuAg alloy nanoparticles and the conservation of the targets' stoichiometry during laser ablation, the element composition of 10 different nanoparticles contained in the polymer matrix were analyzed by FE-STEM-EDXS (Fig. 7). The average atomic content of silver and gold in the nanoparticles obtained is 50.9 ± 2.7 % Ag and 49.1 ± 2.7 % Au, with only 3 % deviation from the target composition (47.0 % Ag and 53.0 % Au).

3.5 Tuning of alloy composition and optical properties

Laser irradiation of metallic flakes [47, 48], or photoreduction of metallic salts has been used in the last years for the preparation of nanoparticles in solution. The same procedure can be used for the generation of alloy nanoparticles by irradiation of colloidal mixtures [36, 49, 50]. The mixtures, from which extinction spectra are shown in Fig. 8, have been irradiated for 15 min with the same laser parameters as the ablation process. Regardless of the concentration of the Au atomic ratio in the colloid, the two-maxima UV-Vis spectra changed to a single plasmon (dashed lines), positioned between the corresponding Au and Ag plasmon peaks of the initial solution (solid lines). It has been determined experimentally and theoretically that the plasmon peak shifts linearly from the Ag resonant wavelength to the Au resonant wavelength as the Au/Ag ratio within nanoparticles increases [37, 51, 52]. This has been attributed to the proportional variation of the high frequency dielectric function of the alloy with respect to the molar ratio of the material components [37]. Hence, linear regression over the plasmon wavelength of the Au and Ag nanoparticles allows for the determination of the atomic composition of the nanoparticles resulting from laser ablation of AuAg alloys. The inset in Fig. 8 shows the linear regression of the plasmon resonant wavelengths of each colloidal solution. The dashed line of the spectra shown in Fig. 8 indicates the plasmon resonant wavelength of the alloy nanoparticles (467 nm) that, according to the linear fit, have an atomic composition of approximately 42 % Au and 57 % Ag. This deviates 10 % from the

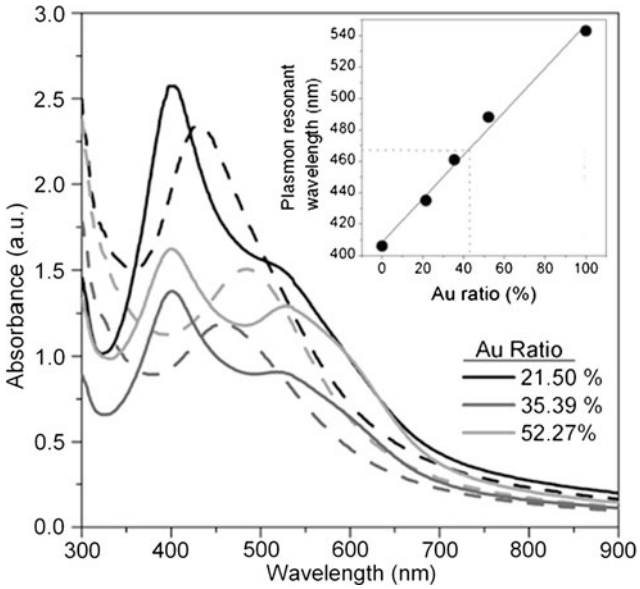

Fig. 8 Extinction spectra of three mixtures of laser-generated Au and Ag colloids with different atomic concentration ratios in MMA (*solid lines*). The *dashed lines* show the spectra of the corresponding colloids after laser irradiation. In the *inset*, the plasmon resonant wavelength of gold and silver nanoparticles and irradiated mixtures of Au and Ag colloids are plotted. The *dotted line* (*inset*) indicates the plasmon resonant wavelength of the nanoparticles generated by laser ablation of an Au/Ag-alloy, and the corresponding particle atomic composition

alloy composition. The possible disparity in the values may be due to the different nanoparticle sizes in each sample. The excellent correlation of the experimental data with the linear regression indicates that alloy nanoparticles are also formed after the irradiation process.

4 Conclusion

Plasmon-resonant thermoplastic polymers have a broad application potential in injection-moldable optical components. Using metal and alloy nanoparticles and mixtures thereof would allow tuning the optical properties by mixing of the respective plasmon resonances. For prototyping of such materials synthesis of the plasmon-resonant nanoparticles by a precursor and stabilizer-free method directly in presence of the monomer gives access to matrix-binder-free nanoparticle composites.

We have demonstrated that Au, Ag, and AuAg-alloy PMMA nanocomposites can be produced by laser ablation of a solid target in the liquid monomer MMA. The small hydrodynamic diameters of the nanoparticles in the monomer (<50 nm) point out that nanoparticles are finely dispersed and isolated in the liquid phase directly after the generation process. Nevertheless, the UV-Vis spectra indicate that particle aging occurs in the colloidal state. The TEM images show interparticle distances of several nanometers. Most likely, the MMA molecules prevent the contact between nanoparticles sterically, thereby avoiding aggregation, and agglomerates only of roughly 100 nm secondary diameter are formed by the primary nanoparticles in the colloid with time. We cannot rule out the possibility that polymerization of the MMA monomers may occur locally because of local heating induced by laser-light absorption by the nanoparticles. It is, however, very difficult to experimentally distinguish an adsorbed layer of PMMA from a layer of unpolymerized monomers.

Since no chemical precursors are required for the generation of nanoparticles using the laser ablation technique, nanocomposites free of matrix binders benefit from this technique. Moreover, the rapid bleaching recovery of nanoparticles via fragmentation (on the order of ns [53]) and tunable absorption band of alloy nanoparticles are advantages of nanoparticle polymer composites in comparison with using typical dyes. We have achieved transferring the optical properties of the colloidal nanoparticles to the solid nanocomposite, with uniform embedding into the whole polymer volume, so that colloids in a monomer with tunable element composition are produced and the thermoplastic polymer is ready to be used for further processing (e.g., injection molding [30] or electrospinning [54]). Complementary to the laser ablation of the solid alloy, we have shown that nanoalloys can also be fabricated by appropriate mixing of Ag and Au nanoparticles in monomer and subsequent laser irradiation. The absorption band of the colloid can be tuned between 400 and 600 nm simply by selection of the ratio of the initial Au and Ag colloids or target.

Acknowledgements We thank the "Investitions- und Förderbank Niedersachsen—NBank" for financial support under the project W3-80019725 and the Institute for Physical Chemistry and Electrochemistry of Leibniz University, Hannover, for the FE-STEM-EDXS analysis of AuAg nanoparticles, and D.D. van't Zand for help during the manuscript's revision.

References

1. S. Misra, P. Mathur, M. Yadav, M. Tiwari, S. Garg, P. Tripathi, Polymer **45**(25), 8623–8628 (2004)
2. M. Wang, X. Wang, Polymer **49**(6), 1587–1593 (2008)
3. Y. Li, S. Fu, Y. Mai, Polymer **46**(6), 2127–2132 (2006)
4. T. Kashiwagi, E. Grulke, J. Hilding, K. Groth, R. Harris, K. Butler, J. Shields, S. Kharchenko, J. Douglas, Polymer **45**(12), 4227–4239 (2004)
5. T. Kashiwagi, F. Du, J. Douglas, K. Winey, R. Harris, J. Shields, Nat. Mater. **4**(12), 928–933 (2005)
6. H. Koerner, G. Price, N. Pearce, M. Alexander, R. Vaia, Nat. Mater. **3**(2), 115–120 (2004)
7. J. Smith, J. Connell, D. Delozier, P. Lillehei, K. Watson, Y. Lin, B. Zhou, Y. Sun, Polymer **45**(3), 825–836 (2004)
8. A. Pomogailo, V. Kestelman, *Metallopolymer Nanocomposites* (Springer, Berlin, 2005)
9. E.T. Thostenson, C. Li, T.W. Chou, Compos. Sci. Technol. **65**(3–4), 491–516 (2005)
10. A. Kabashin, M. Meunier, J. Appl. Phys. **94**(12), 7941–7943 (2003)
11. T. Tsuji, K. Iryo, N. Watanabe, M. Tsuji, Appl. Surf. Sci. **202**(1–2), 80–85 (2002)
12. S.C. Singh, R. Gopal, J. Phys. Chem. C **112**(8), 2812–2819 (2008)
13. W.T. Nichols, T. Sasaki, N. Koshizaki, J. Appl. Phys. **100**(11), 114912-1–114912-6 (2006)
14. F. Mafune, J. Kohno, Y. Takeda, T. Kondow, H. Sawabe, J. Phys. Chem. B **105**(22), 5114–5120 (2001)
15. F. Mafune, J. Kohno, Y. Takeda, T. Kondow, J. Phys. Chem. B **107**(18), 4218–4223 (2003)
16. J. Sylvestre, A. Kabashin, E. Sacher, M. Meunier, J. Luong, J. Am. Chem. Soc. **126**(23), 7176–7177 (2004)
17. G. Compagnini, A.A. Scalisi, O. Puglisi, J. Appl. Phys. **94**(12), 7874–7877 (2003)
18. S. Barcikowski, M. Hustedt, B. Chichkov, Polimery **53**(9), 657–662 (2008)
19. F. Grohn, B. Bauer, Y. Akpalu, C. Jackson, E. Amis, Macromolecules **33**(16), 6042–6050 (2000)
20. V. Chechik, R. Crooks, Langmuir **15**(19), 6364–6369 (1999)
21. A. Semerok, C. Chaleard, V. Detalle, J.L. Lacour, P. Mauchien, P. Meynadier, C. Nouvellon, B. Salle, P. Palianov, M. Perdrix, G. Petite, Appl. Surf. Sci. **139**, 311–314 (1999)
22. B.N. Chichkov, C. Momma, S. Nolte, F. vonAlvensleben, A. Tunnermann, Appl. Phys. A, Mater. Sci. Process. **63**(2), 109–115 (1996)
23. G. Ledoux, D. Amans, C. Dujardin, K. Masenelli-Varlot, Nanotechnology **20**(44), 445605 (2009)
24. T. Trelenberg, L. Dinh, B. Stuart, M. Balooch, Appl. Surf. Sci. **229**(1–4), 268–274 (2004)
25. S. Petersen, S. Barcikowski, Adv. Funct. Mater. **19**(8), 1167–1172 (2009)
26. V. Zaporojtchenko, R. Podschun, U. Schuermann, A. Kulkarni, F. Faupel, Nanotechnology **17**(19), 4904–4908 (2006)
27. A. Hahn, S. Guenter, P. Wagener, S. Barcikowski, J. Mater. Chem. **21**(28), 10287–10289 (2011)
28. A. Wang, Y. Hsieh, Y. Chen, C. Mou J. Catal. **237**(1), 197–206 (2006)
29. L. Polavarapu, N. Venkatram, W. Ji, Q.H. Xu, ACS Appl. Mater. Interfaces **1**(10), 2298–2303 (2009)
30. P. Wagener, G. Brandes, A. Schwenke, S. Barcikowski, Phys. Chem. Chem. Phys. **13**(11), 5120–5126 (2011)
31. J. Jakobi, A. Menendez-Manjon, Chakravadhanula, K. Venkata Sai, L. Kienle, P. Wagener, S. Barcikowski, Nanotechnology **22**(14), 145601 (2011)
32. J. Jakobi, S. Petersen, A. Menendez-Manjon, P. Wagener, S. Barcikowski, Langmuir **26**(10), 6892–6897 (2010)
33. S. Barcikowski, A. Menendez-Manjon, B. Chichkov, M. Brikas, G. Raciukaitis, Appl. Phys. Lett. **91**(8), 083113 (2007)
34. E. Hecht, *Optics* (Addison-Wesley, Reading, 2002)
35. E. Cottancin, J. Lerme, M. Gaudry, M. Pellarin, J. Vialle, M. Broyer, B. Prevel, M. Treilleux, P. Melinon, Phys. Rev. B, Condens. Matter **62**(8), 5179–5185 (2000)

36. G. Compagnini, E. Messina, O. Puglisi, V. Nicolosi, Appl. Surf. Sci. **254**(4), 1007–1011 (2007)
37. P. Mulvaney, Langmuir **12**(3), 788–800 (1996)
38. J.F. Sanchez-Ramirez, U. Pal, L. Nolasco-Hernandez, J. Mendoza-Alvarez, J.A. Pescador-Rojas, J. Nanomater. **2008**, 620412 (2008)
39. E. Roberts, K. Clarke, R. Hunt, Mater. Sci. Eng. **42**(1–2), 71–80 (1980)
40. A. Schwenke, P. Wagener, S. Nolte, S. Barcikowski, Appl. Phys. A, Mater. Sci. Process. **104**, S77–S82 (2011)
41. V. Bogatyrev, L. Dykman, B. Khlebtsov, N. Khlebtsov, Opt. Spectrosc. **96**(1), 128–135 (2004)
42. S. Barcikowski, A. Hahn, A.V. Kabashin, B.N. Chichkov, Appl. Phys. A, Mater. Sci. Process. **87**(1), 47–55 (2007)
43. T. Tsuji, K. Iryo, Y. Nishimura, M. Tsuji, J. Photochem. Photobiol. A, Chem. **145**(3), 201–207 (2001)
44. S. Besner, A.V. Kabashin, M. Meunier, Appl. Phys. Lett. **89**(23), 233122 (2006)
45. A. Takami, H. Kurita, S. Koda, J. Phys. Chem. B **103**(8), 1226–1232 (1999)
46. P. Mulvaney, L. Liz-Marzan, M. Giersig, T. Ung, J. Mater. Chem. **10**(6), 1259–1270 (2000)
47. M. Kawasaki, N. Nishimura, Appl. Surf. Sci. **253**(4), 2208–2216 (2006)
48. D. Werner, S. Hashimoto, T. Tomita, S. Matsuo, Y. Makita, J. Phys. Chem. C **112**(5), 1321–1329 (2008)
49. J. Zhang, J. Worley, S. Denommee, C. Kingston, Z.J. Jakubek, Y. Deslandes, M. Post, B. Simard, N. Braidy, G.A. Botton, J. Phys. Chem. B **107**(29), 6920–6923 (2003)
50. Z. Peng, B. Spliethoff, B. Tesche, T. Walther, K. Kleinermanns, J. Phys. Chem. B **110**(6), 2549–2554 (2006)
51. M. Zhou, S. Chen, S. Zhao, H. Ma, Physica E **33**(1), 28–34 (2006)
52. L. Liz-Marzan, Langmuir **22**(1), 32–41 (2006)
53. P.V. Kamat, M. Flumiani, G.V. Hartland, J. Phys. Chem. B **102**(17), 3123–3128 (1998)
54. D.D. 't Zand van, P. Nachev, R. Rosenfeld, P. Wagener, A. Pich, D. Klee, S. Barcikowski, J. Laser Micro Nanoeng. **7**(1), 21–27 (2012)